Functional Impact of Nth-like DNA glycosylase on Mitochondrial Dynamics

Lisa Hubers[1], Alexander Myr Sjetne[1], Luisa Luna[1], Ane Marit Wågbø[3], Yohan Lefol[1,2], Francisco Jose Naranjo Galindo[1], Anders Knoph Berg-Eriksen[1], Torkild Visnes[3], Hilde Nilsen[1,2] and Nicola P. Montaldo[1,2¤]

[1] Department of Microbiology, Oslo University Hospital and University of Oslo, 0424 Oslo, Norway.
[2] Cresco Centre for Embryology and Healthy Development.
[3] Department of Biotechnology and Nanomedicine, SINTEF Industry, 7034 Trondheim, Norway.

¤ Correspondent author:
Nicola P. Montaldo
tel: +47 45394916
e-mail: n.p.montaldo@medisin.uio.no

ABSTRACT
Nth-like DNA glycosylase (NTHL1) is a base excision repair enzyme, with a crucial role both in nuclear and mitochondrial genomic maintenance. In this study, we demonstrate a key function of NTHL1 on mitochondrial DNA (mtDNA) maintenance and mitochondrial dynamics. Our results reveal significant accumulation of mitochondrial transcripts and increased mtDNA levels in NTHL1-deficient cells, accompanied by an accumulation of mtDNA lesions. These findings underscore the essential role of NTHL1 in protecting against mitochondrial genomic damage. In addition to increased OXPHOS mRNA and protein levels, Seahorse analyzer measurements further demonstrated enhanced mitochondrial respiratory capacity and elevated oxygen consumption rates. Furthermore, NTHL1 deficiency was associated with increased mitochondrial size and elevated protein levels of the mitochondrial fusion protein Dynamin-like GTPase OPA1, mitochondrial, long form (L-OPA1). Notably, NTHL1 knockout cells showed resistance to 1-methyl-4-phenylpyridinium (MPP+)-induced mitochondrial stress, indicating that the loss of NTHL1 promotes mitochondrial resilience and an adaptive response to oxidative stress. Combined, these findings indicate a complex phenotype where in NTHL1 plays a multifaceted role in mitochondrial maintenance and its loss leads to mild mitochondrial dysfunction that activates mitohormesis. This study thus extends the known functions of NTHL1 beyond nuclear DNA repair, highlighting its critical role in mitochondrial health and regulation of cellular resilience to oxidative stress.

INTRODUCTION

DNA base lesions occur frequently in cells due to exposure to both endogenous and exogenous DNA-damaging agents[1]. Among the various forms of damage, oxidized bases are particularly detrimental, necessitating efficient repair mechanisms to maintain genomic integrity. Base excision repair (BER) is the primary pathway for repair of such lesions in DNA[2].

The BER pathway involves several critical steps: Initially, a damaged base is recognized and excised by a DNA glycosylase ´, generating an apurinic/apyrimidinic (AP) site. This AP site is subsequently processed by apurinic/apyrimidinic endonuclease 1 (APE1) or by the endonuclease activity of bifunctional DNA glycosylases. Next, DNA polymerase β fills in the single-strand break, and finally, DNA ligase III/XRCC1 seals the nick. In *Escherichia coli* (*E. coli)*, Endonuclease III (Nth) DNA glycosylase recognizes various pyrimidine base damages. This enzyme has been evolutionarily conserved to humans. Both bacterial Nth and its human counterpart Nth-like DNA glycosylase, NTHL1 (also referred as hNTHL1 or NTH1), contain a helix-hairpin-helix (HhH) domain, essential for DNA binding, as well as an [4Fe-4S] cluster. NTHL1, cloned and characterized in 1997[3], showed substrate specificity that closely resembled that of bacterial Nth. In fact, NTHL1 is a bifunctional DNA glycosylase, plays a key role in this process by recognizing and removing oxidized purine bases such as 2,6-diamino-4-hydroxy-5-formamidopyrimidine (FapyG) and 2,6-diamino-4-hydroxy-5-formamidopyrimidine (FapyA), as well as oxidized pyrimidine bases like thymine glycol (Tg). Additionally, NTHL1 is capable of identifying and cleaving AP sites.

Mitochondria are vital for cellular energy production, signaling, and apoptosis Mitochondrial dysfunctions play a crucial role in the onset of neurodegenerative disorders, just as in aging. The integrity of mtDNA is crucial for proper mitochondrial function, as it encodes essential components of the oxidative phosphorylation (OXPHOS) system. Importantly, despite the high susceptibility of mtDNA to damage due to its proximity to the electron transport chain mitochondria have relatively limited DNA repair mechanisms compared to nuclear DNA[4], and understanding the role of NTHL1 in mtDNA maintenance is of significant interest. Recent studies indicate that BER enzymes may also play crucial roles in maintaining and regulating mitochondrial DNA (mtDNA) integrity, particularly considering the relative scarcity of other DNA repair mechanisms within the organelle (reviewed in [4]).

mtDNA copy number (mtDNA-CN) is typically associated with energy production and storage, oxidative stress levels, and mitochondrial membrane potential[5]. Studies using knockdown cell models with reduced mtDNA-CN have shown decreased mitochondrial protein expression, changes in cellular morphology, and diminished respiratory enzyme activity, highlighting the connection between mtDNA-CN and mitochondrial function [6]. Several studies have quantified mtDNA-CN in tissues from individuals across various ages. Ding et al. (2015) reported an age-related decline in mtDNA levels, measured in lymphocytes from over 2,000 Sardinian participants[7]. Furthermore, in aging population, a lower mtDNA-CN has been associated with a progressive cognitive and physical decline and with a higher mortality risk [8]. Lower mtDNA-CN has been associated with prevalent frailty in white participants and is a strong predictor of all-cause mortality[9]. Therefore, understanding the mechanisms of mtDNA-CN regulation is crucial, as it is a key determinant of mitochondrial function and cellular energy production. Variations in mtDNA-CN can significantly impact cellular health, especially in high-energy-demand tissues such as neurons.

Recent research highlights how changes in mtDNA-CN levels correlate with mitochondrial dysfunction, cognitive decline, and disease progression, and may influence therapeutic outcomes (reviewed in [10]). A significant association between reduced mtDNA-CN and Parkinson's disease (PD) suggests that decreased mtDNA content may be implicated in PD pathogenesis and could hold prognostic value in predicting disease progression [11]. Longitudinal changes in mtDNA-CN are associated with PD progression and dopaminergic treatment [12]. Recent research suggests a complex interplay between BER, oxidative stress, and mitochondrial dysfunction in PD pathology. BER has been implicated in the age-dependent accumulation of single-stranded DNA breaks, contributing to PD pathology in a *C. elegans* model [13]. In this system, the human ortholog NTH-1 plays a role in genomic instability and neurodegeneration in aging organisms, whereas its loss is associated with a protective phenotype characterized by reduced proteotoxicity [13].

In this study, we investigate the impact of NTHL1 deficiency on mtDNA integrity and mitochondrial function. Our findings reveal a substantial increase in mtDNA levels and the accumulation of mtDNA lesions in NTHL1-deficient cells. This increase in mtDNA is accompanied by enhanced mitochondrial transcriptional output, reflected in elevated levels of OXPHOS mRNA and proteins. Furthermore, Seahorse Analyzer measurements showed that NTHL1-deficient cells exhibit increased mitochondrial oxygen consumption rates, indicating enhanced respiratory capacity. This suggests that NTHL1 deficiency may improve the mitochondria's ability to generate energy (ATP), which is crucial for cellular functions and may play a role in the observed protective effects. Additionally, we examine the effects of NTHL1 deficiency on the expression of key mitochondrial regulatory proteins. Our results show that NTHL1 deficiency correlates with increased levels of the long form of the fusion protein Dynamin-like GTPase OPA1, mitochondrial (L-OPA1), suggesting a complex regulatory network involving NTHL1 and mitochondrial function. Importantly, NTHL1 knockout cells exhibited resistance to mitochondrial stress induced by complex I inhibitor 1-methyl-4-phenylpyridinium (MPP+) [14-18], further suggesting that the loss of NTHL1 promotes mitochondrial resilience and an adaptive response to oxidative stress.

These findings expand our understanding of the critical role of NTHL1 in maintaining mitochondrial health, Moreover, these observations align with our hypothesis that the observed changes are part of a mitohormesis response, where moderate mitochondrial stress induces beneficial cellular adaptations, enhancing resilience and function.

RESULTS

NTHL1 localizes in the mitochondria

The human NTHL1 protein features an extended N-terminal segment of approximately 95 residues[3,19], which contains a mitochondrial targeting sequence (MTS) and three predicted nuclear localization signals (NLSs) located within or adjacent to this region (PLRRR at 30, PVKRPRK at 46, PKVRR at 117). Consistently, NTHL1 was previously shown to be present in mitochondria[20]. However, according to NCBI, NTHL1 has three isoforms of NTHL1 (Fig. 1A). Among these, we observed that isoform 1 exhibited the highest expression levels, whereas transcripts of isoforms 2 and 3 were detected at lower levels, as illustrated by RT-qPCR experiments (Fig. 1B). This was confirmed by RT-PCR using primers capable of amplifying all three isoforms, or specific primers targeting each individual isoform (Fig. S1A and 1B, C respectively). Given the uncertainty of whether removing only isoform 1 would lead to compensatory expression of the other isoforms, we used the CRISPOR tool to design single-guide RNA (sgRNA) to target all three NTHL1 isoforms (Fig. 1A) in HEK293 cells via CRISPR/Cas9 technology [21]. iFollowing transfection with NTHL1-specific sgRNAs and Cas9 nuclease, individual clones were isolated for further analysis. Clonal cell lines were initially screened using an indel-specific PCR, which does not produce a PCR product in the presence of indel mutations (Fig. S2A). Clones showing no amplification in the indel-specific PCR were considered potential knockouts (Fig. S2B). These clones were further validated by Sanger sequencing of the region surrounding the sgRNA target site, confirming the presence of indel mutations (Fig. S2C). Disruption of the NTHL1 gene at protein level was then confirmed through immunoblotting (Fig. 1C) and subsequently used for further experiments. Sanger sequencing further confirmed the occurrence of Indel mutations in the NTHL1 gene in selected knockout clones, confirming successful gene disruption at the protein level (Fig. S1F). To ensure specificity, off-targets that could arise from sgRNA unspecific annealing were predicted using CRISPOR. Top candidates targeting exon regions were ruled out by indel-specific PCR and Sanger sequencing of the amplified off-target sites (Fig. S2D-F). DNA glycosylase activity of NTHL1 was further assessed to validate the successful knockout of the NTHL1 gene. A significant reduction of glycosylase activity in NTHL1 knockout cells, compared to WT controls, provided confirmation of the knockout (Fig. 1D).

Saccharomyces cerevisiae NTHL1 ortholog, Ntg1 is dynamically regulated in response to either nuclear and/or mitochondrial oxidative DNA damage[22]. The human NTHL1, has a disordered structure in the N-terminal region [23] which contains nuclear and mitochondrial localization sequences [20,24,25]. A previous study identified the amino acid sequences 29–34, 44–49, 28–52, and 47–51 as putative nuclear localization signals (NLS) [26]. Immunofluorescence analysis of HBEC-3KT cells overexpressing wild-type HA-NTHL1 and N-terminal deletion constructs revealed that, unlike the wild type and other mutants, the Δ42–60 mutant exhibits heterogeneous localization between the nuclear and cytoplasmic compartments, with potential localization in mitochondria as well[26].

To verify the mitochondrial localization of NTHL1, we performed cell compartment fractionation. Our results showed that NTHL1 localizes to the cytosolic (C), mitochondrial (M), and nuclear (N) fractions (Fig. 1E, lanes 2, 3, and 4, respectively). We observed that the majority of NTHL1 was localized in the nucleus, with a smaller molecular weight band observed mainly in the mitochondria. To confirm the signal specificity for NTHL1, the same experiment was performed in NTHL1-deficient cell lines, which showed no detectable signal

(Fig. 1E, lanes 5–8). Furthermore, to verify that the lower molecular weight band observed in the mitochondrial fraction represented a processing product of full-length NTHL1, we transfected the knockout cell lines with a vector expressing NTHL1. This reintroduced NTHL1 produced the same localization pattern, confirming that the lower molecular weight band in the mitochondrial fraction corresponded to a processed form of NTHL1.

RNA Sequencing Analysis Reveals Altered Mitochondrial Gene Expression in NTHL1 Knockout (KO) Cell Lines

To identify whether loss of NTHL1 has an impact on the mRNA levels of genes involved in mitochondrial dynamics, we performed RNA sequencing (RNA-seq) on wild type (WT) and *NTHL1*$^{-/-}$ cell lines (Fig. 2A). Differentially expressed genes (DEGs) identified by comparative transcriptomics, with a log2 fold change threshold of +/-1.0 and False discovery rate (FDR) ≤ 0.05, were filtered using MitoCarta 3.0 to identify mitochondrial-relevant genes. This analysis revealed that the mRNA levels of 68 mitochondrial-related genes were altered in *NTHL1*$^{-/-}$ cell lines compared to WT (Fig. 2A). Subsequent gene ontology (GO) enrichment analysis performed using g:Profiler [27] indicated that most DEGs in *NTHL1*$^{-/-}$ cell lines were associated with oxidoreductase activity as a molecular function (adjusted p-value 6.329×10^{-19}) (Fig. 2B). The DEGs were also enriched for biological processes such as the small molecule metabolic process and the respiratory electron transport chain (adjusted p-values 6.329×10^{-19} and 1.660×10^{-17}, respectively) (Fig. 2B and fig. S2). The RNA sequencing results were confirmed by RT-qPCR measurements of mRNA levels for multiple regulated genes belonging to the top identified biological processes presented in Fig. 2B. To validate the RNA sequencing results, RT-qPCR was conducted, confirming that mRNA levels of HCCS and TSPO were significantly upregulated in NTHL1$^{-/-}$ cells, while FASN and ALDH1L2 were downregulated (Fig. 2G).

Identification of Functional Clusters of Mitochondrial-Related Genes Altered in *NTHL1*$^{-/-}$ Cell Lines

To further explore the functional relationships among the mitochondrial-related genes affected by NTHL1 loss, we performed a STRING analysis (full STRING network). This analysis allowed us to identify key interaction networks among the differentially expressed mitochondrial genes, which were grouped into four distinct clusters. Cluster 1 was the largest, comprising 29 genes and was primarily associated with mitochondrial functions crucial for energy production. This cluster was significantly enriched for genes involved in the aerobic electron transport chain and oxidoreduction-driven active transmembrane transporter activity, both critical for mitochondrial respiration and ATP synthesis. The alterations in these processes suggest that NTHL1 knockout affects mitochondrial electron transport, leading to altered energy metabolism (Fig. 3A and B). Cluster 2 (gene count: 9) included genes involved in fatty acid catabolism and arachidonate-CoA ligase activity, which are essential for mitochondrial lipid metabolism (Fig. 3A and C). This finding suggests that NTHL1 deficiency might impact energy metabolism and fatty acid utilization and storage. In addition to these main clusters, two smaller clusters were identified: Cluster 3 (gene count: 3) was associated with protein maturation by iron-sulfur cluster transfer, and Cluster 4 (gene count: 2) was linked to tRNA methyltransferase activity, a process crucial for mitochondrial protein synthesis. Alterations in this cluster point to potential defects in mitochondrial translation and protein maturation in *NTHL1*$^{-/-}$ cells. Hence, NTHL1 deficiency affects multiple mitochondrial processes, including energy production, and fatty acid metabolism.

NTHL1 deficiency causes increased mitochondrial DNA copy number

Among the DEGs detected in Fig. 2, several mitochondrially encoded genes displayed increased transcription levels (Fig. 3A, B). Given that mitochondrial gene expression is tightly linked to mitochondrial function, we reasoned that this overall upregulation might be a compensatory response to mitochondrial dysfunction, potentially driven by an increase in mitochondrial biogenesis or a response to elevated oxidative stress. mtDNA copy number (mtDNA-CN) has long been recognized as a biomarker for mitochondrial dysfunction [28]. Analysis of mtDNA-CN in HEK293 cells revealed a 2-fold increase in mtDNA-CN in *NTHL1*$^{-/-}$ cell lines compared to WT cells (Fig. 3C).

To investigate mtDNA integrity in NTHL1-deficient cells, we employed two complementary qPCR-based methods to quantify DNA damage. First, we used the Real-time qPCR Analysis of Damage Frequency (RADF) assay[29], which involves the restriction enzyme TaqI, recognizing the sequence 5'-TCGA-3'. In the presence of a lesion near or at this site, the enzyme's ability to cleave the DNA is inhibited. Amplification following enzyme digestion provides a quantitative measure of DNA damage at these specific sites. In NTHL1-deficient cells, the RADF assay revealed increased mtDNA damage, reflecting the presence of lesions that block enzymatic digestion (Fig. 3D). Second, we performed long-amp qPCR, a method designed to amplify long fragments of mtDNA. DNA damage impairs polymerase activity, leading to reduced amplification. In NTHL1-deficient cells, we observed a significant reduction in amplification compared to wild-type controls, indicating higher levels of mtDNA lesions (Fig. 3E). The impaired amplification of longer fragments suggests that the polymerase was impeded by DNA damage, further supporting the findings from the RADF assay. Together, these results consistently show that NTHL1-deficient cells exhibit elevated mtDNA damage.

Loss of NTHL1 causes increased mitochondrial respiration

To investigate whether reduced mtDNA integrity affected mitochondrial function we measured metabolic activity using the Seahorse XF Cell Mito Stress Assay. The average basal mitochondrial oxygen consumption rate (OCR)in *NTHL1*$^{-/-}$ cell lines was on average 80% higher than in WT cells (Fig. 4A, B). This positive trend was also evident for mitochondrial OCR sensitive to the ATPase inhibitor oligomycin, where the OCR coupled to ATP production was significantly elevated in *NTHL1*$^{-/-}$ cells compared to WT cells (see OCR after addition of oligomycin in Fig. 3a, and bars in Fig. 4C). Moreover, when mitochondria were stressed by permeabilizing the inner membrane for H^+ with carbonyl cyanide 4-(trifluoromethoxy) phenylhydrazone (FCCP) to reveal maximal mitochondrial respiratory capacity, the responsive increase in OCR of *NTHL1*$^{-/-}$ cell mitochondria were on average 2 times higher compared to WT cells (see OCR after addition of FCCP in Fig. 3A and bars in Fig. 4D). Additionally, the spare respiratory capacity was significantly increased in *NTHL1*$^{-/-}$ cells (see OCR after addition of Rotenone and Antimycin in Fig. 3A and bars in Fig. 4E). These findings suggest that the absence of NTHL1 enhances mitochondrial respiratory activity and overall mitochondrial efficiency. This enhancement could be a compensatory response to increased mtDNA damage observed in *NTHL1*$^{-/-}$ cells, implying that while NTHL1 is essential for maintaining mtDNA integrity, its absence triggers adaptive mechanisms to sustain mitochondrial function and energy production.

Furthermore, the Seahorse analysis revealed that NTHL1 deficient lines showed increased proton leak and non-mitochondrial oxygen consumption (Fig. S3A, B). Increased proton leak suggests that more protons (H^+) are crossing the mitochondrial membrane independently of

ATP production resulting in a "leak" of energy as heat, bypassing the ATP synthase. Non-mitochondrial oxygen consumption reflects the oxygen consumed by reactions outside the mitochondria. These reactions could include oxidase activities, such as NADPH oxidases or other enzymes that generate reactive oxygen species (ROS). An increase in non-mitochondrial oxygen consumption suggests enhanced oxidative activity occurring outside of mitochondrial respiration, possibly due to increased ROS production. Increased non-mitochondrial oxygen consumption could indicate heightened oxidative stress or increased activity of oxygen-consuming processes outside the mitochondria, such as ROS generation. Taken together, these observations indicate that the cells are undergoing a mild oxidative stress response, which may be driving adaptive changes in cellular metabolism and energy production. This shift can be interpreted as mitohormesis, where moderate mitochondrial stress enhances cellular resilience and function. This interpretation aligns with previous observations showing that NTH-1 loss enhances resilience in a *C.elegans* model [13].

Loss of NTHL1 results in increased oxidative phosphorylation protein levels and mitochondrial size

To further understand the role of NTHL1 in regulating mitochondrial function, we first measured the levels of proteins belonging to the oxidative phosphorylation (OXPHOS) pathway. Using immunoblotting, we observed an increase in the levels of these proteins in NTHL1 deficient cells, consistent with our gene expression studies (Fig. 6A, B). To further characterize the impact of NTHL1 loss, we used transmission electron microscopy (Fig. 6C) to investigate mitochondrial morphology. Interestingly, *NTHL1*$^{-/-}$ cells did not show a change in the number of mitochondria per cell (Fig. 6D) but rather an increase in mitochondrial size (Fig. 6E). This observation suggests that alterations in mitochondrial mass may be affected. To this end, we performed immunoblotting for mitochondrial fusion proteins. We observed an increase in the protein levels Dynamin-like GTPase OPA1, mitochondrial, specifically the long form (L-OPA1) (Fig. 6F, G), a mitochondrial inner membrane fusion protein that plays a central role in mitochondrial inner membrane fusion and cristae morphology [14-18]. Notably, knockout of OPA1 in fibroblasts has previously been shown to result in decreased mtDNA levels [30]. Interestingly, our results showed no significant differences in the protein levels of either Mitofusin 1 (MFN1) and Mitofusin 2 (MFN2) — other key mitochondrial outer membrane proteins that mediate mitochondrial fusion— between *NTHL1*$^{-/-}$ and WT cells (Fig. X). This indicates that the absence of NTHL1 does not influence the expression of these key mitochondrial fusion proteins.

Taken together, these findings suggest that the loss of NTHL1 leads to enhanced mitochondrial fusion which is dependent on L-OPA1, thereby contributing to increased mitochondrial size.

NTHL1 Loss decreases sensitivity to Complex I inhibition

If the changes observed were indeed part of a mitohormesis response, we would expect that the *NTHL1*$^{-/-}$ cells would exhibit differences in their response to mitochondrial stress due to the observed increase in OXPHOS-related proteins in these cells. Given that MPP+ is a mitochondrial toxin known to inhibit mitochondrial complex I (NADH oxidoreductase) in the electron transport chain [31-33], we hypothesized that NTHL1 deficiency might alter the cellular response to MPP^+-induced mitochondrial dysfunction. MPP+ disrupts electron flow by inhibiting complex I, reducing ATP production, and increasing reactive oxygen species (ROS), leading to oxidative stress and cellular damage, particularly in mitochondria-dependent cells

like neurons. Consistent with our hypothesis, NTHL1 deficient cells exhibited enhanced tolerance to MPP+ compared to WT cells. After 72 hours of MPP+ treatment, WT cells showed a significant reduction in cell numbers, while *NTHL1*$^{-/-}$ cells maintained stable cell counts across various MPP+ concentrations (Fig. 7A-B). This suggests that NTHL1 deficiency confers resistance to MPP+-induced mitochondrial stress. Interestingly, MPP+ treatment did not induce significant cell death in either WT or *NTHL1*$^{-/-}$ cells, as indicated by the minimal increase in propidium iodide-positive cells (Fig. 7C). This finding implies that the reduction in WT cell numbers is likely due to impaired cell proliferation rather than apoptosis or necrosis. In contrast, *NTHL1*$^{-/-}$ cells were largely unaffected, supporting the idea that NTHL1 may regulate pathways involved in mitochondrial stress response and cell proliferation under conditions of complex I inhibition.
Furthermore, cell viability was decreased in both WT and *NTHL1*$^{-/-}$ cells following MPP+ treatment, but *NTHL1*$^{-/-}$ cells maintained significantly higher viability than WT cells at all tested concentrations (Fig. 7D). Consistent results were also observed using HAP1 cell lines (Fig. S4). This further indicates that NTHL1 deficient cells are more resilient to MPP+-induced mitochondrial dysfunction, potentially due to improved oxidative phosphorylation (OXPHOS) capacity or alternative metabolic pathways that mitigate the effects of complex I inhibition.

DISCUSSION

In this study, we investigated the impact of the DNA glycosylase NTHL1 on mitochondrial dynamics and function. Our findings provide new insights into how NTHL1 deficiency affects mitochondrial integrity, respiratory activity, and cellular resilience, revealing a role in mitochondrial health beyond its established function in nuclear DNA repair.

Our results demonstrate that loss of NTHL1 in HEK293 cells leads to significant accumulation of mtDNA, accompanied by increased mtDNA lesions and elevated transcription of OXPHOS-related genes. The observed accumulation of mtDNA lesions in NTHL1-deficient cells underscores its critical role in mtDNA repair and homeostasis. NTHL1 is a DNA glycosylase known to remove oxidized purines and pyrimidines from DNA evidenced by the fact that mitochondrial repair activity for oxidative pyrimidines was observed in mtDNA of rats [34,35]. Our data suggest that NTHL1 contributes to the repair of oxidative mtDNA damage, and its absence leads to a compromised mtDNA repair capacity. This finding aligns with previous studies demonstrating the presence of NTHL1 in mitochondria and its involvement in mtDNA repair activity. Interestingly, despite the accumulation of mtDNA damage, NTHL1-deficient cells exhibited elevated mtDNA copy number. This could be attributed to a compensatory response to counteract the detrimental effects of mtDNA damage. Increased mtDNA-CN has been documented in response to various mitochondrial stresses while reduced mtDNA-CN has been observed in patients affected by numerous neurodegenerative diseases, including PD, during both the early stages and later in disease progression [28,36]. It is conceivable that cells lacking NTHL1 attempt to elevate mtDNA levels to maintain a functional mitochondrial pool by increasing the availability of undamaged mtDNA molecules for transcription and translation.

Interestingly, the increase in mitochondrial oxygen consumption rates and enhanced respiratory capacity observed in Seahorse Analyzer assays also implies a compensatory adaptation that improves the energy-generating capability of mitochondria despite the accumulation of damage. This adaptive response is consistent with the concept of

mitohormesis, in which moderate mitochondrial stress activates protective mechanisms that promote cellular resilience and improved function.

One of the key observations of our study is that NTHL1 deficiency leads to increased mitochondrial size and elevated protein levels of the mitochondrial inner membrane fusion protein, long form OPA1 (L-OPA1). OPA1 is critical for mitochondrial fusion and cristae maintenance, processes that contribute to enhanced mitochondrial efficiency and the stability of the electron transport chain. Our data imply that increased OPA1 levels may drive the enhanced mitochondrial fusion observed in NTHL1-deficient cells, resulting in larger mitochondria that are potentially more capable of managing oxidative stress. In contrast, no significant changes were observed in the levels of Mitofusin 1 (MFN1) or Mitofusin 2 (MFN2), mitochondrial outer membrane proteins involved in mediating mitochondrial fusion. This suggests that NTHL1 selectively influences the mitochondrial fusion machinery through OPA1 while not affecting MFN1 and MFN2, pointing to a specific role in regulating inner mitochondrial membrane fusion.

Another significant finding is the resistance of NTHL1-deficient cells to mitochondrial stress induced by the complex I inhibitor MPP+. MPP+ is known to induce mitochondrial dysfunction by inhibiting NADH oxidoreductase, leading to decreased ATP production and increased ROS generation [18,31-33]. Interestingly, NTHL1 knockout cells demonstrated enhanced tolerance to MPP+-induced stress. These observations indicate that the absence of NTHL1 activates protective pathways that confer resilience to mitochondrial stress. We hypothesize that this resilience may be related to the increased respiratory capacity observed in these cells, as well as potential alternative metabolic adaptations that mitigate the impact of complex I inhibition. Importantly, the enhanced resistance to MPP+ also suggests a link between NTHL1 deficiency and altered mitochondrial stress signaling, which could have implications for understanding neurodegenerative diseases such as PD, where mitochondrial dysfunction plays a central role. These finding are supported by previous literature, as Interactions between BER gene variants and pesticide exposure have been associated with increased PD risk [37]. Furthermore our results align with observation in a *C.elegans* PD model of α-synuclein expression in which *nth-1* mutants exhibit similar resistance to MPP+ and other mitochondrial stressors[13]. This reinforces the notion that BER deficiency might promote adaptive mitochondrial resilience, suggesting a conserved mechanism across species.

Collectively, our findings extend the role of NTHL1 beyond nuclear DNA repair and demonstrate its critical importance in maintaining mitochondrial health and regulating adaptive responses to oxidative stress. The observed phenotype of NTHL1-deficient cells — characterized by increased mtDNA copy number, elevated OXPHOS activity, and resistance to mitochondrial stress— highlights the complex interplay between DNA repair, mitochondrial function, and cellular resilience. The concept of mitohormesis, where moderate mitochondrial stress induces beneficial cellular adaptations, provides a framework for understanding how loss of NTHL1 can enhance mitochondrial function despite an apparent increase in DNA damage. This adaptation may be particularly relevant in the context of aging and neurodegeneration, where mitochondrial dysfunction is a hallmark feature.

ACKNOWLEDGMENTS

This research was supported in part by the Michael J. Fox Foundation to H.L.N and N.P.M. (project no. #022355) and by the Research Council of Norway (project no. #302483) through its Centres of Excellence scheme (project no. 332713). We extend our gratitude to Veronica Suaste Morales for her assistance with the quality control of the high-throughput data. We are also deeply grateful to Professor Lars Aide for his valuable help and insightful discussions.

AUTHOR CONTRIBUTIONS

L.H.: Investigation, Validation, Writing – original draft, Writing.
A.M.S, L.L., Y.L., V.S:M., F.J.N.G, A.M.W, A.K:B: Investigation, Validation.
N.P.M, H.L.N, T.V.: Conceptualization, Supervision, Writing – original draft, Writing.

DECLARATION OF INTERESTS

The authors declare no competing interests.

FIGURES AND FIGURE LEGENDS

Figure 1

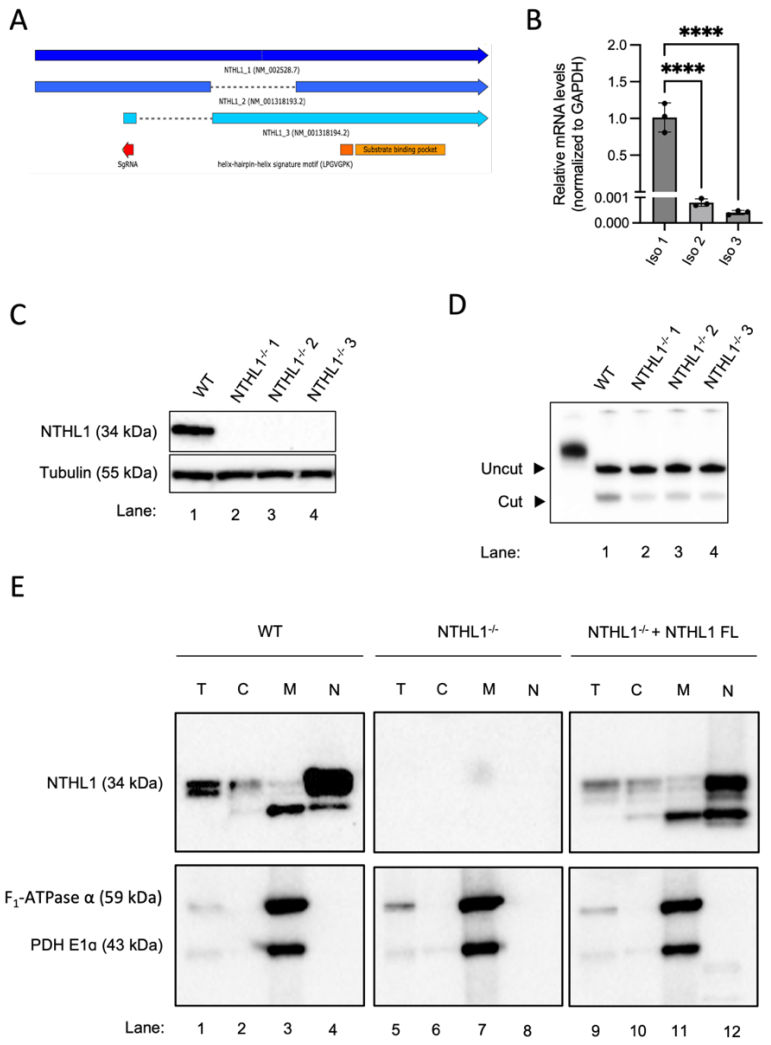

Figure 1: NTHL1 localises in mitochondria

(A) Schematic representation of the CRISPR-Cas9 design. The cut site (red) is shown in relation to the exons (blue) on all three isoforms of NTHL1. Since the cut is upstream of the substrate-binding pocket, the resulting protein is non-functional.

(B) Relative mRNA levels of NTHL1 isoforms in HEK293 WT cells, indicating that isoform 1 is the most prevalent form.

(C) Immunoblot analysis confirming the successful knockout of NTHL1 protein in HEK293 cells. Lane 1 represents WT cells, and lanes 2-4 represent independent *NTHL1*$^{-/-}$ clones.

(D) DNA glycosylase activity assay confirming the loss of activity in *NTHL1-/-* cells. Lane 1 represents WT cells, and lanes 2-4 represent independent *NTHL1*$^{-/-}$ clones.

(E) Fractionation of HEK293 cells shows that endogenous (Lanes 1-4) or exogenous (Lanes 9-12) NTHL1 localizes predominantly to the nucleus, with a smaller molecular weight band observed in the mitochondria. No signal was observed in the *NTHL1*$^{-/-}$ cells (Lanes 5-8). T: Total fraction; C: Cytosolic fraction; M: Mitochondrial fraction; N: Nuclear fraction.

Error bars represent mean ± SD ($n \geq 3$). ****$p \leq 0.0001$, one-way ANOVA.

Figure 2

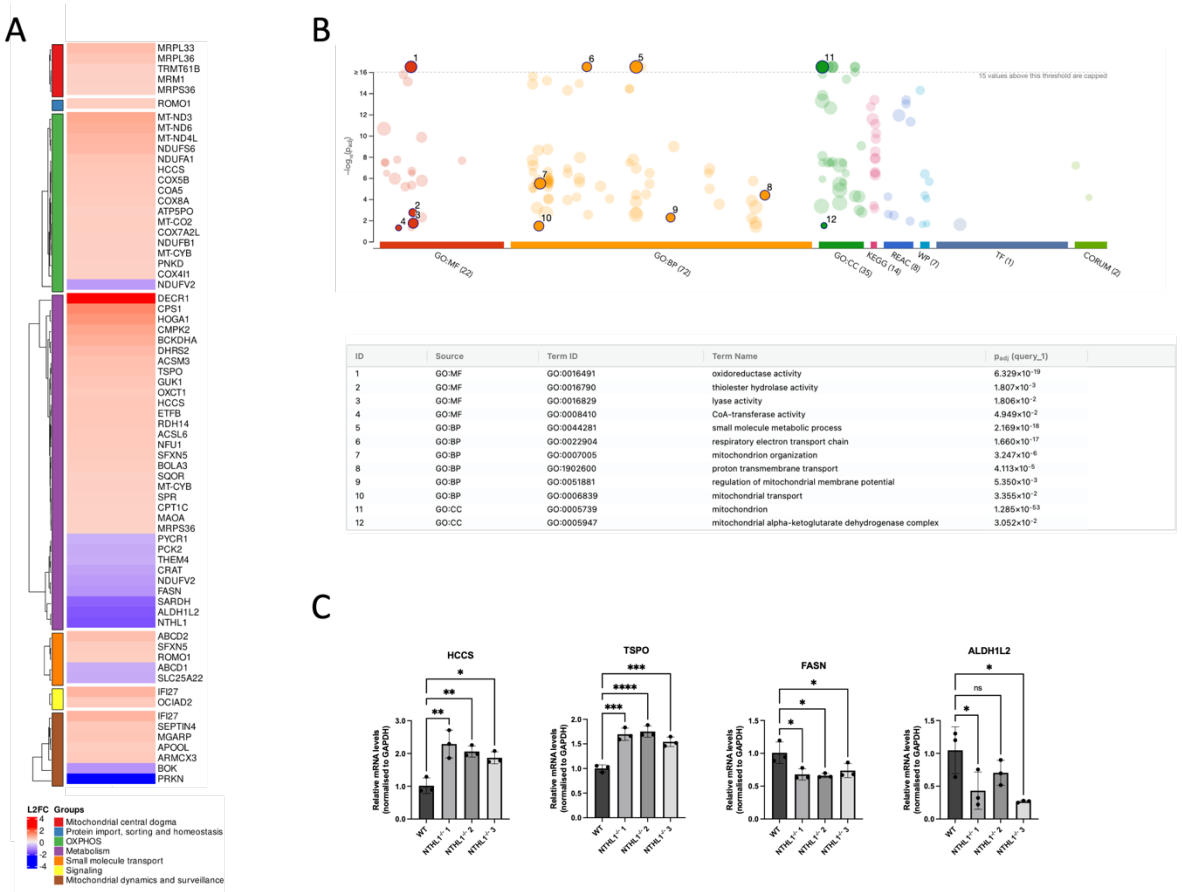

Figure 2: Impact of NTHL1 knockout on mitochondrial gene expression in HEK293 cells.
(**A**) Differentially Expressed Genes (DEGs) Identified by RNA-Seq: Heatmap showing DEGs identified by RNA-sequencing (RNA-seq) in WT and *NTHL1*$^{-/-}$. Red colored boxes indicate significantly upregulated genes, and blue boxes indicate significantly downregulated genes in *NTHL1*$^{-/-}$ cells compared to WT (log2 fold change threshold +/-1.0, FDR ≤ 0.05).
(**B**) GO Enrichment Analysis: A bar graph shows the top enriched GO terms associated with the identified mitochondrial DEGs. The x-axis represents the GO term (biological process or molecular function), and the y-axis represents the adjusted p-value (FDR). Significantly enriched terms are highlighted (adjusted p-value < 0.05).
(**C**) RT-qPCR Validation of RNA-seq Data: RT-qPCR analysis confirms the differential expression of selected upregulated downregulated genes identified by RNA-seq. Data are represented as fold change in *NTHL1*$^{-/-}$ cells relative to WT cells.
Error bars represent mean ± SD (n ≥ 3). *p ≤ 0.001; **p ≤ 0.01; ****p ≤ 0.0001, one-way ANOVA.

Figure 3

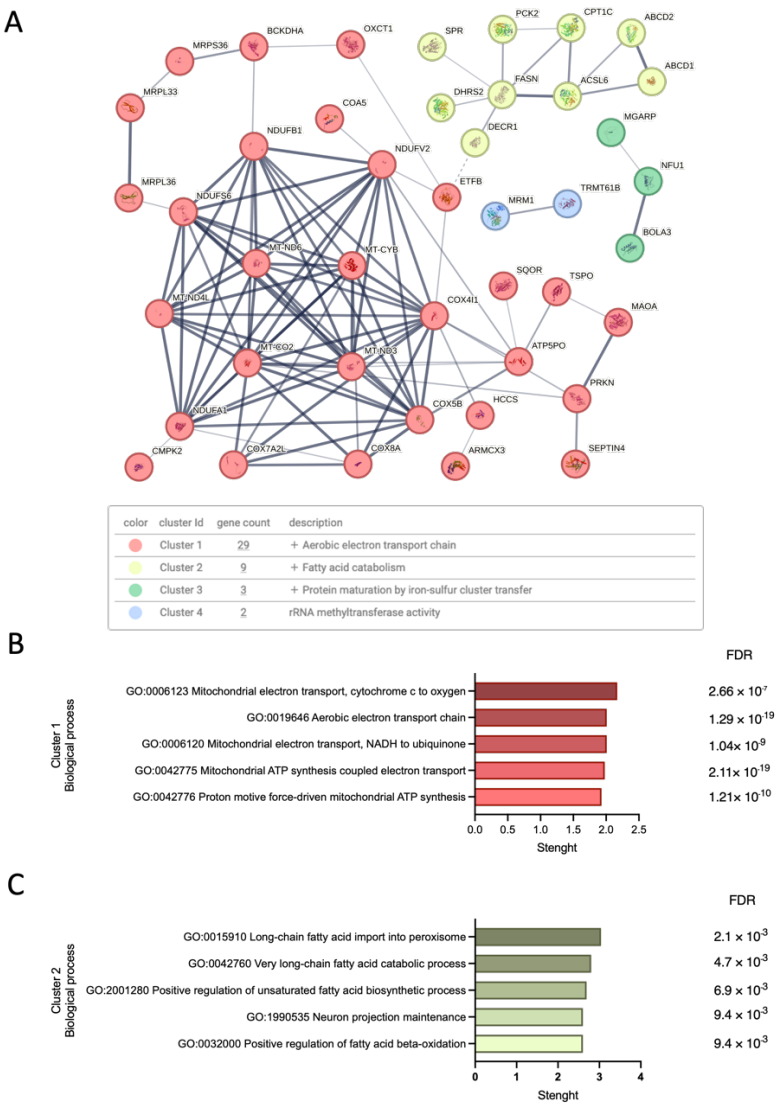

Figure 3: Network analysis and Gene Ontology (GO) Analysis of Mitochondrial-Related Genes Altered in *NTHL1*$^{-/-}$ Cell Lines

(A) STRING network analysis of differentially expressed mitochondrial-related genes in *NTHL1*$^{-/-}$ cell lines. Network is subdivided in four clusters (depicted in red, light green, blue and dark green) through k-means clustering, with the members that characterize each cluster presented. Edge thickness is representative of interaction confidence, based on the experimental evidence, and text mining. Minimum interaction score medium confidence of 0.400

(B) Gene Ontology (GO) enrichment analysis for biological processes (represented with strength as a scale) shows significant enrichment for terms related to aerobic electron transport chain and oxidoreductase activity in Cluster 1.

(C) GO analysis of biological processes related to Cluster 2 highlights significant enrichment for processes involved in fatty acid metabolism, lipid catabolism, and arachidonate-CoA ligase activity, with strength represented on a scale

FDR: false discovery rate

Figure 4

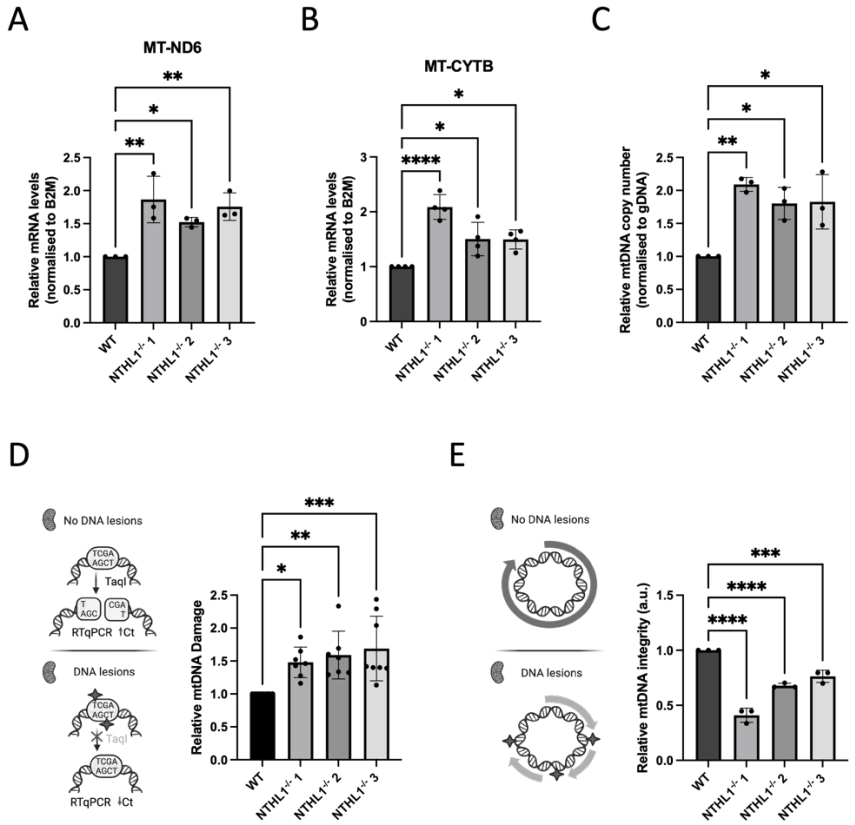

Figure 4: *NTHL1*$^{-/-}$cells show increased mitochondrial RNA and mitochondrial DNA copy number.

(**A,B**) Relative mRNA levels of MT-ND6 (**A**) and MT-CYTB (**B**), genes in HEK293T WT, and *NTHL1*$^{-/-}$ cells.

(**C**) Relative mtDNA copy number in HEK293T WT, and *NTHL1*$^{-/-}$ cell**. The values are normalized to nDNA.**

(**D,E**) mtDNA damage measured with the Real-time qPCR Analysis of Damage Frequency (RADF) assay (**d**), and long-amplicon quantitative PCR (**e**) in HEK293T WT, and *NTHL1*$^{-/-}$ cells. Error bars represent mean ± SD ($n \geq 3$). *$p \leq 0.05$; **$p \leq 0.01$; ****$p \leq 0.0001$, one-way ANOVA.

Figure 5

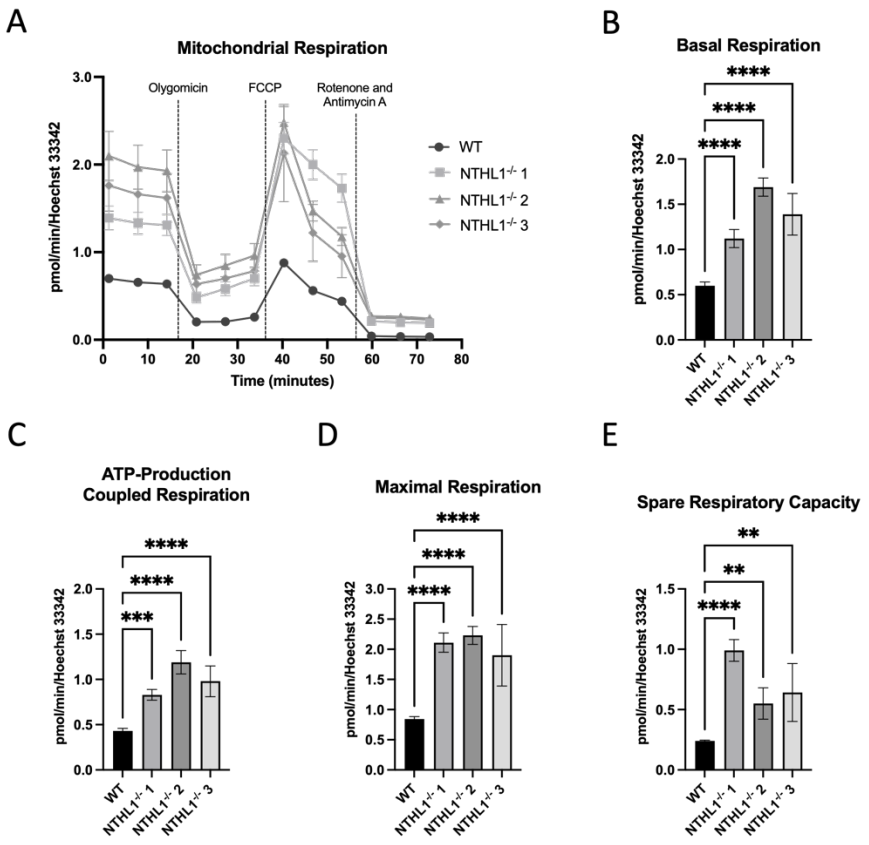

Figure 5: Mitochondrial energy metabolism is enhanced *NTHL1*$^{-/-}$cells.
Bioenergetics of HEK293 WT and *NTHL1*$^{-/-}$ cell lines were assessed using the Seahorse Flux Analyzer with the Cell Mito Stress Kit.
(**A**) mitochondrial oxygen consumption curves are presented as averages ± standard deviations for each measurement time point (n = 5). The initial three measurement points represent basal mitochondrial respiration. The following three points, after the addition of oligomycin to block adenine nucleotide translocation, represent proton leak-stimulated oxygen consumption. Next, three points represent maximal mitochondrial oxygen consumption capacity, achieved by uncoupling the mitochondrial inner membrane with FCCP. The final three points measure non-mitochondrial oxygen consumption when the mitochondrial respiratory chain is inhibited by rotenone and antimycin A.
(**B**) Summary data for basal respiration.
(C) Summary data of ATP-Production coupled respiration.
(**D**) Summary data for maximal respiration.
(**E**) Summary data for spare respiratory capacity. Error bars represent mean ± SD (n = 5). **p ≤ 0.01; ***p ≤ 0.001; ****p ≤ 0.0001, one-way ANOVA.

Figure 6

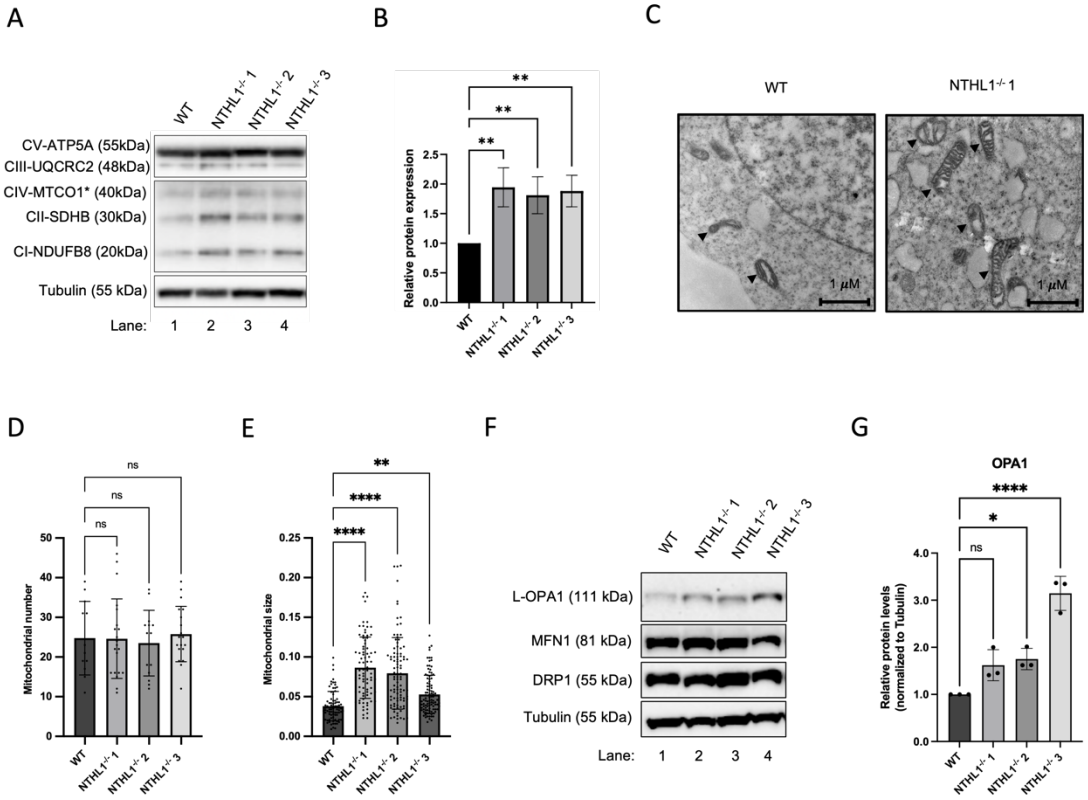

Figure 6: Loss of NTHL1 increases OXPHOS protein levels and promotes mitochondrial fusion.

(**A**) Immunoblot analysis of OXPHOS complex proteins in WT and *NTHL1*$^{-/-}$ cells. Increased protein levels of all OXPHOS complexes were observed in NTHL1-deficient cells compared to WT cells.

(**B**) Quantification of total OXPHOS protein levels from immunoblots. Data are represented as fold change in *NTHL1*$^{-/-}$ cells relative to WT cells .

(**C**) Representative transmission electron microscopy (TEM) images of WT and *NTHL1*$^{-/-}$ cells. Scale bar = 2 µm.

(**D**) Quantification of mitochondrial number per cell from TEM images. No significant difference in the number of mitochondria between WT and *NTHL1*$^{-/-}$ cells was observed.

(**E**) Quantification of mitochondrial size from TEM images. Mitochondrial area was measured for at least 100 mitochondria per cell. NTHL1-deficient cells exhibited significantly larger mitochondria compared to WT cells.

(**F**) Immunoblot analysis of OPA1 protein levels in WT and *NTHL1*$^{-/-}$ cells. Increased OPA1 protein levels were detected in *NTHL1*$^{-/-}$ cells compared to WT cells.

(**G**) Quantification of OPA1 protein levels from immunoblots. Data are represented as fold change in *NTHL1*$^{-/-}$ cells relative to WT cells. Error bars represent mean ± SD ($n \geq 3$). *$p \leq 0.05$; **$p \leq 0.01$; ****$p \leq 0.0001$, one-way ANOVA.

Figure 7

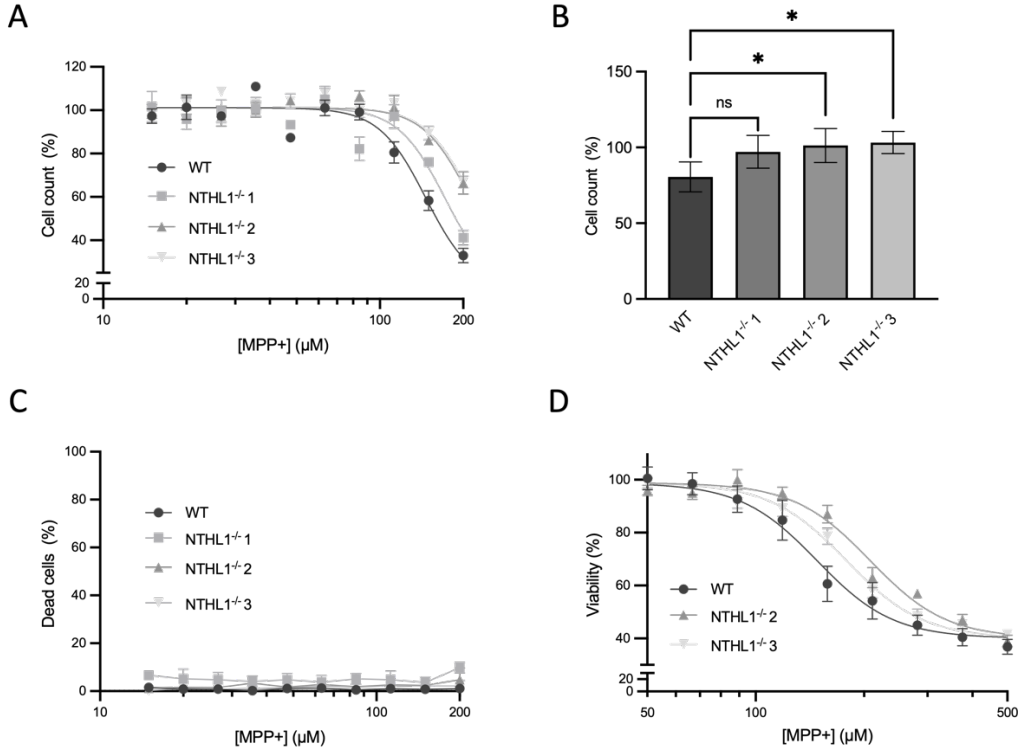

Figure 7: NTHL1-deficient cells display enhanced tolerance to 1-methyl-4 phenylpyridinium (MPP+).

(A-B) MPP+ treatment reduces cell numbers in WT but not *NTHL1*$^{-/-}$ cells. WT and *NTHL1*$^{-/-}$ cells were exposed to the indicated concentrations of MPP+ for 72 h, stained with Hoechst 33342 and the number of cells in each wells counted. Data represent average ± SD (n=8 technical replicates, representative of n=2 independent experiments).

(C) MPP+ treatment does not induce cell death. WT and *NTHL1*$^{-/-}$ cells were exposed to the indicated concentrations of MPP+ for 72 h, stained with Hoechst 33342 and propidium iodide, and the percentage of propidium iodide-positive cells in each well calculated. Data represent average ± SD (n=8 technical replicates, representative of n=2 independent experiments).

(D) MPP+ treatment decreases viability. WT and *NTHL1*$^{-/-}$ cells were exposed to the indicated concentrations of MPP+ for 72 h, and viability was assessed with Cell-titer glo. Data represent average ± SD (n=4 technical replicates, representative of n=2 independent experiments).

METHODS

Cell Culture

Human embryonic kidney cells (HEK293, American Tissue Culture Collection, CRL-1573™) were cultured at 37°C under a 5% CO_2 atmosphere in Dulbecco's Modified Eagle Medium (DMEM) high glucose medium (Gibco) supplemented with 10% fetal bovine serum serum (FBS) and 1% penicillin/streptomycin (P/S). HAP1 cells were cultured at 37°C under a 5% CO_2 atmosphere in Iscove's Modified Dulbecco's Medium (IMDM) (Gibco) supplemented with 10% FBS and 1% P/S.

Long-term storage

Cells were cryopreserved using a standard liquid nitrogen (N2) storage protocol. Briefly, cells were harvested and washed with PBS before being resuspended in IMDM for HAP1 or DMEM for HEK293 medium containing 20% FBS and 10% dimethyl sulfoxide (DMSO) as a cryoprotectant. The cell suspensions were aliquoted into cryotubes and initially storet at -80°C to allow gradual cooling. The following day, cryotubes were transferred to N2 for long-term storage.

Generation of HEK293 Knockout cell lines

short guide RNAs (sgRNAs) targeting NTHL1 gene were designed using the CRISPR Design tools CRISPOR [21]. Alt-R® CRISPR/Cas9 tracrRNA ATTO™550 was initially resuspended in Nuclease-Free Duplex Buffer to a concentration of 100 µM. Guide (crRNA) was combined in a 1:1 ratio with the tracrRNA and annealed by heating at 95°C for 5 minutes, followed by a slow cooling process at room temperature. The resulting single guide RNA (sgRNA) complexes were then diluted 1:100 in Opti-MEM (Gibco™) to achieve a concentration of 1 µM. Alt-R® S.p. Cas9 Nuclease V3 (from IDT) was diluted to 1 µM in Opti-MEM immediately prior to use. CRISPR/Cas9 components were delivered to HEK293 WT using Lipofectamine™ 3000 Transfection Reagent (Invitrogen™). Upon transfection cells were seeded as single clones into a 96-well plate via serial dilution. Insertion-deletion (Indel) mutations and loss of target protein expression were verified in clonal knockout cell lines through Indel specific PCR, sanger sequencing and immunoblot analysis, respectively. To ensure specificity, potential off-target mutations in *NTHL1*$^{-/-}$ cells were ruled out by sequencing top-candidate off-target sites predicted using CRISPOR.

Generation of HAP1 Knockout cell lines

In this study the following HAP1 (or K562) cell lines were used: WT 1.1, WT 1.3, NTHL1 KO 10, NTHL1 KO 11. These cell lines were a gift from Magnar Bjøras and were originally generated by Horizon Discovery (PerkinElmer company).

Indel specific PCR

DNA extracted with Qiagen AllPrep was amplified in a PCR reaction (Promega Gotaq G2 Master mix 2X (Promega, M7822) 25uL, 2.5uL Fw primer, 2.5uL Rv primer, 12.5 DNA (10 ng/uL), 7.5 uL nuclease-free water), and run on a 1% agarose gel. The forward primer was designed to have its last base anneal to the base after the CRISPR-Cas9 cut site. Thus, the Taq Polymerase does not elongate the substrate in most cases of Indel mutations. This causes a heavily reduced or absent amplicon, leading to a yes/no readout from the gel.

Sanger sequencing

PCR reaction (Promega Gotaq G2 Master mix 2X (Promega, M7822) 25uL, 2.5uL Fw primer, 2.5uL Rv primer, 12.5 DNA (10 ng/uL), 7.5 uL nuclease-free water), and run on a 1% agarose gel. The correct band is excised using UV light, and then purified with NucleoSpin Gel and PCR Clean-up (Macherey-Nagel, 740609.250). This is then sent to Eurofins Light run with a single primer near the loci of interest for Sanger sequencing.

Off-targets assessment

The two most likely off-targets of the sgRNA were controlled by Indel specific PCR, and Sanger sequencing. The two off-targets were DCTN1 and MAST3, with 2 and 3 base pair differences compared with the sgRNA respectively.

Gene Expression Analysis

RNA was purified using the Qiagen RNeasy kit following the manufacturer's protocol, including DNase digestion (QIAGEN) to remove genomic DNA contamination. Subsequently, reverse transcription was carried out using Qiagen MultiScribe Reverse Transcriptase according to manufacturer's instructions. Quantitative PCR (qPCR) was conducted using Power SYBR PCR Master Mix (Applied Biosystems) on a StepOnePlus v2.3 Real-Time PCR System. Relative transcription levels were determined by normalizing to B2M mRNA levels. Primer sequences used in the qPCR analysis are listed in Supplemental Materials.

Library Construction, Quality Control, and Sequencing

Total RNA was purified with RNeasy kit (QIAGEN), and DNaseI digested (QIAGEN) according to the manufacturer's protocol. Total RNA was used as the input material for RNA sample preparations. RNA library preparation, and sequencing, were carried out by Novogene Europe. Ribosomal RNA (rRNA) was removed from total RNA using specific probes. RNA fragmentation was performed using divalent cations at elevated temperatures in the First Strand Synthesis Reaction Buffer. First-strand cDNA was synthesized using random hexamer primers and reverse transcriptase. The second strand of cDNA was then synthesized by adding buffer and dNTPs, where dTTP was replaced by dUTP. The synthesized double-stranded cDNA was subjected to end repair, A-tailing, adaptor ligation, and PCR enrichment following fragment selection. To select cDNA fragments ranging from 370-420 bp, PCR products were purified using AMPure XP beads, resulting in a strand-specific library. Following library construction, preliminary quantification was performed using Qubit. The size of the inserted fragments was evaluated, and the library's effective concentration was quantified using qRT-PCR. The qualified libraries were then pooled and sequenced on Illumina platforms according to the required effective concentration and data output. The original fluorescence image files generated by the Illumina platform were converted into short reads (raw data) through base calling. The resulting short reads were stored in FASTQ format [38].

RNAseq processing

Quality control was applied to the raw reads to eliminate sequence artifacts, such as adapter contamination, low-quality nucleotides, and unrecognizable nucleotides (N). Quality control was performed using Fastp (v0.23.1) [39]. The quality of clean reads was assessed using FastQC (v0.11.9) prior to alignment. Reads were aligned to the human reference genome (GRCh38) from Ensembl release 109[40] using STAR (v2.7.10b)[41], with corresponding gene annotations from the same Ensembl release. Gene-level counts were generated during alignment by

enabling the --quantMode GeneCounts option in STAR. For downstream analyses, counts from the fourth column of the STAR output, corresponding to the reverse-stranded library orientation, were used.

RNAseq analysis

Counts were normalized and processed using DESeq2 (DESeq2 1.40.2)[42]. Genes with an absolute log 2 fold change of 1 or more as well as a false discovery rate smaller than 0.05 were treated as significant differentially expressed genes (DEGs). DEGs were clustered using the PART algorithm [43], with parameters of recursion set to 100 and a minimum cluster size of 50 genes. The seed was set to '123456' for reproducibility purposes. Each cluster wast then submitted to gprofiler (gprofiler2 version 0.2.2)[44].

DNA Copy Number Analysis

DNA was isolated from cell extracts using the Qiagen AllPrep kit according to manufacturer's protocol. To digest any remaining RNA, samples were incubated with 10 µg/mL Ribonuclease A and incubated for 1 hour at 37C. DNA was collected by ethanol precipitation, and qPCR was carried out using Power SYBR PCR Master Mix as above. All primers are listed in Supplemental Materials. To determine the mtDNA/genomic DNA ratio, amplification of individual genes from the mitochondrial genome were compared to a gene from the nuclear genome (B2M).

RADF qPCR DNA Damage Assay

qPCR was performed as described previously, with and without Taq1 restriction enzyme. Primers, which are listed in Supplemental Materials, are specific to the mitochondrial genome and contain a Taq1 restriction site. DNA damage frequency was calculated as (2^-) difference between the Taq1-treated and non-treated genomic DNA.

Mitochondrial DNA damage via Long-Amp PCR

To assess the frequency of DNA lesions capable of inhibiting polymerase activity, we employed the long-amplicon quantitative polymerase chain reaction (LA-QPCR) assay previously described [45]. The underlying principle is that the presence of DNA lesions will reduce the efficiency of PCR amplification, with the extent of amplification inversely correlating with the number of lesions within the DNA template. For each reaction, a master mix was prepared containing 25 µL of LongAmp Hot Start Taq2X Master Mix(NEW ENGLAND Biolabs, M0533L), 15 ng of purified DNA template, and 2 µL of each 10 µM primer (forward and reverse) in a final volume of 50 µL. No-template controls (NC) and 50% template controls were included in each experimental run. The 50% template controls were prepared by diluting the DNA template 1:1 with nuclease-free water. PCR was carried out in a thermal cycler under the following conditions: initial denaturation at 94°C for 2 minutes, followed by 17 cycles of 94°C for 15 seconds and 64°C for 12 minutes. The final extension step was performed at 72°C for 10 minutes. After PCR, 10 µL of the product from each reaction was loaded onto a 1% agarose gel, and the electrophoresis was performed. The resulting DNA bands were visualized, and their intensities were quantified using ImageJ software. The fluorescence values obtained from triplicate samples were averaged, and the average value of the no-template control was subtracted from all other samples. It was ensured that the blank-corrected 50% control signal ranged between 40% and 60% of the full template signal.

Each sample's fluorescence value, corrected for the no-template control, was divided by its respective normalized mtDNA copy number. The so normalised values were averaged, and normalised to control sample (WT).

Whole Cell Extraction

Total proteins were extracted from cell pellets using RIPA lysis buffer containing 10mM Tris-HCl, 150mM NaCl, 0.5mM EDTA, 0.1% SDS, 1% Triton X-100 and 1% NaDeoxycholate. Samples were incubated on ice for 30 minutes with frequent pipetting, followed by centrifugation to remove cell debris. The supernatant was removed, proteins were quantified using Bradford Assay and used for further analysis.

Immunoblot Analysis

10-40ug protein extract was combined with Laemmli buffer and incubated for 5 minutes at either 95℃ or 25℃, depending on the antibodies used. Samples were run on a SDS-PAGE gel and transferred to a nitrocellulose membrane. Membranes were blocked in 5% milk followed by incubation with primary antibody, either for 1 hour or overnight. Membranes were incubated with HRP-conjugated secondary antibodies for 30-60 minutes prior to developing. Antibodies used are listed in Supplemental Materials.

Transmission Electron Microscopy

Briefly, cells were fixed in 2.5% glutaraldehyde, stained in 1% osmium tetroxide, and solidified in 1% agar overnight. Agar containing the cell suspension was subjected to graded dehydration in ethanol and propylene oxide before being embedded in Durcupan resin. Ultrathin sections were cut on a Leica RM UC6 ultramicrotome, contrasted with 1% uranyl acetate and 0.3% lead citrate, and left to dry overnight. Sections were placed on an electron microscopy grid and cellular ultrastructure was visualized on the Tecnai 12 biotwin electron microscope.

Bioenergetics Analysis

To evaluate cellular bioenergetics, we conducted oxygen consumption rate (OCR) measurements using a Seahorse Xfe96 analyzer (Seahorse Biosciences, MA, USA) via mito stress. Cells were seeded into a Seahorse microplate at a density of 7×10^4 cells/well and subjected to the specified treatments. Following treatment, cells were equilibrated in DMEM lacking sodium bicarbonate, supplemented with either 5 mmol/L or 35 mmol/L of d-glucose (depending on the treatment), 2 mmol/L of glutamine, and 1 mmol/L of sodium pyruvate. OCR measurements included basal OCR and OCR responses to sequential injections of 1.5 µmol/L oligomycin (an ATP synthase inhibitor targeting mitochondrial complex V), 1 µmol/L FCCP (a mitochondrial uncoupler), and 0.5 µmol/L rotenone/antimycin (inhibitors of mitochondrial complexes I and III, respectively). Parameters such as proton leak, maximal respiration, spare respiratory capacity, non-mitochondrial oxygen consumption, and ATP-linked OCR were analyzed using the mito stress test to assess mitochondrial function. OCR values (pmol O_2/min) were normalized to Hoechst 33342 levels.

Site-Directed Mutagenesis

NTHL1 was sub-cloned from Origene's RG214598 plasmid using restriction digestion, and cloned into Addgene's pcDNA3-RFP plasmid in order to create a C-terminally tagged NTHL1-RFP protein. Site-directed mutagenesis was next used to replace the RFP tag with a FLAG tag,

and later to generate a catalytically dead NTHL1 K220Q mutant as well as deletion mutants lacking 1 or 2 of the nuclear localization sequences (NLSs) from the parent construct (Δ42-60 and Δ21-60 respectively). Primers used are listed in the Supplemental Materials. All plasmids were sequenced for accuracy.

Fractionation Assay

Approximately 3 × 10^6 HEK293 cells were collected and separated into cytoplasmic, mitochondrial and nuclear fractions using Abcam's Cell Fractionation Kit (ab109719) according to manufacturer's protocol. Equal amounts of each fraction were loaded onto an SDS-PAGE gel and run following the immunoblotting protocol described above. Cytochrome c Apoptosis WB Antibody Cocktail was used to confirm separation of the respective fragments.

DNA glycosylase Activity Assay

DNA glycosylase activities were measured using standard assays as previously described [46]. In short, an oligonucleotide containing 5-ohU, was ^{32}P-labeled at the 5' terminus by using T4 polynucleotide kinase (NEB, M0201S) and [γ-^{32}P]ATP (3000 Ci/mmol) (Revvity, NEG502A250UC), and subsequently annealed with the complementary strand containing a normal base opposite the lesion. Reaction mixtures of 10 µl containing 5 fmol of the duplex substrate, reaction buffer (70 mM MOPS, 1 mM DTT, 1 mM EDTA and 5% glycerol) and 10 ug total cell extracts were incubated for 2.5 hours at 37 °C. After addition of 10 µl of stop solution (80% formamide, 10 mM EDTA, bromophenol blue and xylene cyanol), the reaction mixtures were incubated for 10 min at 95 °C. Samples were separated on 20% denaturing polyacrylamide gels and results analyzed using the Amersham Typhoon IP and the ImageQuant IQTL 8.2 software (both from Amersham Biosciences).

Transfection of cultured cells

HEK293 cells were plated 24h prior to transfection at density of approximately 5x10^4 cells/cm^2 achieving 50-70% confluency. Transfection was performed using Lipofectamine 3000 according to manufacturer's protocol. After transfection, cells were incubated for 48 hours before analysis.

Proliferation and viability assay

30 µL HEK293 cells were seeded in 384-well plates (1,800 cells/well) and incubated overnight. Cells were subsequently added a dilution series of MPP+ (Abcam, AB144783) dissolved in medium and further incubated for 72 h. Cells were stained with final volumes 5 µg/ml Hoechst 33342 (Thermo Scientific, 62249) and 1 µM Propidium iodide (Invitrogen, P3566) for 30 minutes and imaged. Image acquisition was performed using the ImageXpress Micro Confocal High-Content Imaging System (Molecular Devices) with a 10× CFI Plan Apochromat Lambda objective and single band dichroic filter sets for imaging Hoechst (Ex. 377/54 nm, Em. 447/60 nm) and Propidium iodide (Ex. 560/32 nm, Em. 624/40 nm). Four fields of view were imaged per well (Approx. 72 % well coverage). Image analysis was conducted with the CellProfilerTM Cell Image Analysis Software 4.2.1. Cell numbers were determined as the number of nuclei stained with Hoechst and dead cells were detected as Propidium iodide positive. Cell viability was measured with the CellTiter-Glo® 2.0 Cell Viability Assay (Promega, G9243) at 25 % final concentration using SPARK® Multimode Microplate Reader (Tecan) to measure luminescence. Cell seeding and MPP+ exposure were identical to the cell counting assay described above.

REFERENCES

1 Lindahl, T. Instability and decay of the primary structure of DNA. *Nature* **362**, 709-715 (1993). https://doi.org:10.1038/362709a0

2 Krokan, H. E. & Bjoras, M. Base excision repair. *Cold Spring Harb Perspect Biol* **5**, a012583 (2013). https://doi.org:10.1101/cshperspect.a012583

3 Aspinwall, R. *et al.* Cloning and characterization of a functional human homolog of Escherichia coli endonuclease III. *Proc Natl Acad Sci U S A* **94**, 109-114 (1997). https://doi.org:10.1073/pnas.94.1.109

4 Akbari, M., Nilsen, H. L. & Montaldo, N. P. Dynamic features of human mitochondrial DNA maintenance and transcription. *Front Cell Dev Biol* **10**, 984245 (2022). https://doi.org:10.3389/fcell.2022.984245

5 Castellani, C. A., Longchamps, R. J., Sun, J., Guallar, E. & Arking, D. E. Thinking outside the nucleus: Mitochondrial DNA copy number in health and disease. *Mitochondrion* **53**, 214-223 (2020). https://doi.org:10.1016/j.mito.2020.06.004

6 Jeng, J. Y. *et al.* Maintenance of mitochondrial DNA copy number and expression are essential for preservation of mitochondrial function and cell growth. *J Cell Biochem* **103**, 347-357 (2008). https://doi.org:10.1002/jcb.21625

7 Ding, J. *et al.* Assessing Mitochondrial DNA Variation and Copy Number in Lymphocytes of ~2,000 Sardinians Using Tailored Sequencing Analysis Tools. *PLoS Genet* **11**, e1005306 (2015). https://doi.org:10.1371/journal.pgen.1005306

8 Mengel-From, J. *et al.* Mitochondrial DNA copy number in peripheral blood cells declines with age and is associated with general health among elderly. *Hum Genet* **133**, 1149-1159 (2014). https://doi.org:10.1007/s00439-014-1458-9

9 Ashar, F. N. *et al.* Association of mitochondrial DNA levels with frailty and all-cause mortality. *J Mol Med (Berl)* **93**, 177-186 (2015). https://doi.org:10.1007/s00109-014-1233-3

10 Cerantonio, A. *et al.* The Role of Mitochondrial Copy Number in Neurodegenerative Diseases: Present Insights and Future Directions. *Int J Mol Sci* **25** (2024). https://doi.org:10.3390/ijms25116062

11 Gui, Y. X., Xu, Z. P., Lv, W., Zhao, J. J. & Hu, X. Y. Evidence for polymerase gamma, POLG1 variation in reduced mitochondrial DNA copy number in Parkinson's disease. *Parkinsonism Relat Disord* **21**, 282-286 (2015). https://doi.org:10.1016/j.parkreldis.2014.12.030

12 Ortega-Vazquez, A. *et al.* Longitudinal Changes in Mitochondrial DNA Copy Number and Telomere Length in Patients with Parkinson's Disease. *Genes (Basel)* **14** (2023). https://doi.org:10.3390/genes14101913

13 SenGupta, T. *et al.* Base excision repair causes age-dependent accumulation of single-stranded DNA breaks that contribute to Parkinson disease pathology. *Cell Rep* **36**, 109668 (2021). https://doi.org:10.1016/j.celrep.2021.109668

14 von der Malsburg, A. *et al.* Structural mechanism of mitochondrial membrane remodelling by human OPA1. *Nature* **620**, 1101-1108 (2023). https://doi.org:10.1038/s41586-023-06441-6

15 Ishihara, N., Fujita, Y., Oka, T. & Mihara, K. Regulation of mitochondrial morphology through proteolytic cleavage of OPA1. *EMBO J* **25**, 2966-2977 (2006). https://doi.org:10.1038/sj.emboj.7601184

16 Anand, R. *et al.* The i-AAA protease YME1L and OMA1 cleave OPA1 to balance mitochondrial fusion and fission. *J Cell Biol* **204**, 919-929 (2014). https://doi.org:10.1083/jcb.201308006

17 Song, Z., Chen, H., Fiket, M., Alexander, C. & Chan, D. C. OPA1 processing controls mitochondrial fusion and is regulated by mRNA splicing, membrane potential, and Yme1L. *J Cell Biol* **178**, 749-755 (2007). https://doi.org:10.1083/jcb.200704110

18 Risiglione, P. *et al.* High-Resolution Respirometry Reveals MPP(+) Mitochondrial Toxicity Mechanism in a Cellular Model of Parkinson's Disease. *Int J Mol Sci* **21** (2020). https://doi.org:10.3390/ijms21217809

19 Hilbert, T. P., Chaung, W., Boorstein, R. J., Cunningham, R. P. & Teebor, G. W. Cloning and expression of the cDNA encoding the human homologue of the DNA repair enzyme, Escherichia coli endonuclease III. *J Biol Chem* **272**, 6733-6740 (1997). https://doi.org:10.1074/jbc.272.10.6733

20 Takao, M., Aburatani, H., Kobayashi, K. & Yasui, A. Mitochondrial targeting of human DNA glycosylases for repair of oxidative DNA damage. *Nucleic Acids Res* **26**, 2917-2922 (1998). https://doi.org:10.1093/nar/26.12.2917

21 Concordet, J. P. & Haeussler, M. CRISPOR: intuitive guide selection for CRISPR/Cas9 genome editing experiments and screens. *Nucleic Acids Res* **46**, W242-W245 (2018). https://doi.org:10.1093/nar/gky354

22 Swartzlander, D. B. *et al.* Regulation of base excision repair: Ntg1 nuclear and mitochondrial dynamic localization in response to genotoxic stress. *Nucleic Acids Res* **38**, 3963-3974 (2010). https://doi.org:10.1093/nar/gkq108

23 Ikeda, S. *et al.* Purification and characterization of human NTH1, a homolog of Escherichia coli endonuclease III. Direct identification of Lys-212 as the active nucleophilic residue. *J Biol Chem* **273**, 21585-21593 (1998). https://doi.org:10.1074/jbc.273.34.21585

24 Ikeda, S., Kohmoto, T., Tabata, R. & Seki, Y. Differential intracellular localization of the human and mouse endonuclease III homologs and analysis of the sorting signals. *DNA Repair (Amst)* **1**, 847-854 (2002). https://doi.org:10.1016/s1568-7864(02)00145-3

25 Luna, L., Bjoras, M., Hoff, E., Rognes, T. & Seeberg, E. Cell-cycle regulation, intracellular sorting and induced overexpression of the human NTH1 DNA glycosylase involved in removal of formamidopyrimidine residues from DNA. *Mutat Res* **460**, 95-104 (2000). https://doi.org:10.1016/s0921-8777(00)00015-x

26 Kar, A., Degtyareva, N. P. & Doetsch, P. W. Human NTHL1 expression and subcellular distribution determines cisplatin sensitivity in human lung epithelial and non-small cell lung cancer cells. *NAR Cancer* **6**, zcae006 (2024). https://doi.org:10.1093/narcan/zcae006

27 Kolberg, L. *et al.* g:Profiler-interoperable web service for functional enrichment analysis and gene identifier mapping (2023 update). *Nucleic Acids Res* **51**, W207-W212 (2023). https://doi.org:10.1093/nar/gkad347

28 Pyle, A. *et al.* Reduced mitochondrial DNA copy number is a biomarker of Parkinson's disease. *Neurobiol Aging* **38**, 216 e217-216 e210 (2016). https://doi.org:10.1016/j.neurobiolaging.2015.10.033

29 Wang, W., Scheffler, K., Esbensen, Y. & Eide, L. Quantification of DNA Damage by Real-Time qPCR. *Methods Mol Biol* **1351**, 27-32 (2016). https://doi.org:10.1007/978-1-4939-3040-1_3

30 Liao, C. *et al.* Dysregulated mitophagy and mitochondrial organization in optic atrophy due to OPA1 mutations. *Neurology* **88**, 131-142 (2017). https://doi.org:10.1212/WNL.0000000000003491

31 Desai, V. G., Feuers, R. J., Hart, R. W. & Ali, S. F. MPP(+)-induced neurotoxicity in mouse is age-dependent: evidenced by the selective inhibition of complexes of electron transport. *Brain Res* **715**, 1-8 (1996). https://doi.org:10.1016/0006-8993(95)01255-9

32 Nicklas, W. J., Vyas, I. & Heikkila, R. E. Inhibition of NADH-linked oxidation in brain mitochondria by 1-methyl-4-phenyl-pyridine, a metabolite of the neurotoxin, 1-methyl-4-phenyl-1,2,5,6-tetrahydropyridine. *Life Sci* **36**, 2503-2508 (1985). https://doi.org:10.1016/0024-3205(85)90146-8

33 Langston, J. W., Ballard, P., Tetrud, J. W. & Irwin, I. Chronic Parkinsonism in humans due to a product of meperidine-analog synthesis. *Science* **219**, 979-980 (1983). https://doi.org:10.1126/science.6823561

34 Driggers, W. J., LeDoux, S. P. & Wilson, G. L. Repair of oxidative damage within the mitochondrial DNA of RINr 38 cells. *J Biol Chem* **268**, 22042-22045 (1993).

35 Driggers, W. J., Holmquist, G. P., LeDoux, S. P. & Wilson, G. L. Mapping frequencies of endogenous oxidative damage and the kinetic response to oxidative stress in a region of rat mtDNA. *Nucleic Acids Res* **25**, 4362-4369 (1997). https://doi.org:10.1093/nar/25.21.4362

36 Asghar, M. *et al.* Mitochondrial biogenesis, telomere length and cellular senescence in Parkinson's disease and Lewy body dementia. *Sci Rep* **12**, 17578 (2022). https://doi.org:10.1038/s41598-022-22400-z

37 Sanders, L. H. *et al.* Editor's Highlight: Base Excision Repair Variants and Pesticide Exposure Increase Parkinson's Disease Risk. *Toxicol Sci* **158**, 188-198 (2017). https://doi.org:10.1093/toxsci/kfx086

38 Cock, P. J., Fields, C. J., Goto, N., Heuer, M. L. & Rice, P. M. The Sanger FASTQ file format for sequences with quality scores, and the Solexa/Illumina FASTQ variants. *Nucleic Acids Res* **38**, 1767-1771 (2010). https://doi.org:10.1093/nar/gkp1137

39 Chen, S., Zhou, Y., Chen, Y. & Gu, J. fastp: an ultra-fast all-in-one FASTQ preprocessor. *Bioinformatics* **34**, i884-i890 (2018). https://doi.org:10.1093/bioinformatics/bty560

40 Martin, F. J. *et al.* Ensembl 2023. *Nucleic Acids Res* **51**, D933-D941 (2023). https://doi.org:10.1093/nar/gkac958

41 Dobin, A. *et al.* STAR: ultrafast universal RNA-seq aligner. *Bioinformatics* **29**, 15-21 (2013). https://doi.org:10.1093/bioinformatics/bts635

42 Love, M. I., Huber, W. & Anders, S. Moderated estimation of fold change and dispersion for RNA-seq data with DESeq2. *Genome Biol* **15**, 550 (2014). https://doi.org:10.1186/s13059-014-0550-8

43 Nilsen, G., Borgan, O., Liestol, K. & Lingjaerde, O. C. Identifying clusters in genomics data by recursive partitioning. *Stat Appl Genet Mol Biol* **12**, 637-652 (2013). https://doi.org:10.1515/sagmb-2013-0016

44 Kolberg, L., Raudvere, U., Kuzmin, I., Vilo, J. & Peterson, H. gprofiler2 -- an R package for gene list functional enrichment analysis and namespace conversion toolset g:Profiler. *F1000Res* **9** (2020). https://doi.org:10.12688/f1000research.24956.2

45 Gonzalez-Hunt, C. P. *et al.* PCR-Based Analysis of Mitochondrial DNA Copy Number, Mitochondrial DNA Damage, and Nuclear DNA Damage. *Curr Protoc Toxicol* **67**, 20 11 21-20 11 25 (2016). https://doi.org:10.1002/0471140856.tx2011s67

46 Hildrestrand, G. A. *et al.* The capacity to remove 8-oxoG is enhanced in newborn neural stem/progenitor cells and decreases in juvenile mice and upon cell differentiation. *DNA Repair (Amst)* **6**, 723-732 (2007). https://doi.org:10.1016/j.dnarep.2006.12.008

SUPPLEMENTARY NOTES

Figure S1

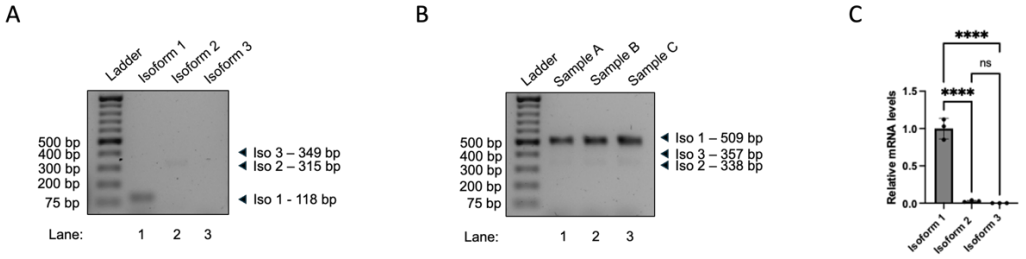

Figure S1: Evaluation of NTHL1 isoforms.
(A-C) PCR analysis of NTHL1 isoforms. Isoform 1 exhibited the highest expression levels, while isoforms 2 and 3 were detected at lower levels.
(A) PCR using specific primers targeting each individual isoform.
(B) PCR using primers capable of amplifying all three isoforms. Isoform 1 exhibited the highest expression levels, while isoforms 2 and 3 were detected at lower levels.
(C) Quantification of experiment depicted in B

Figure S2

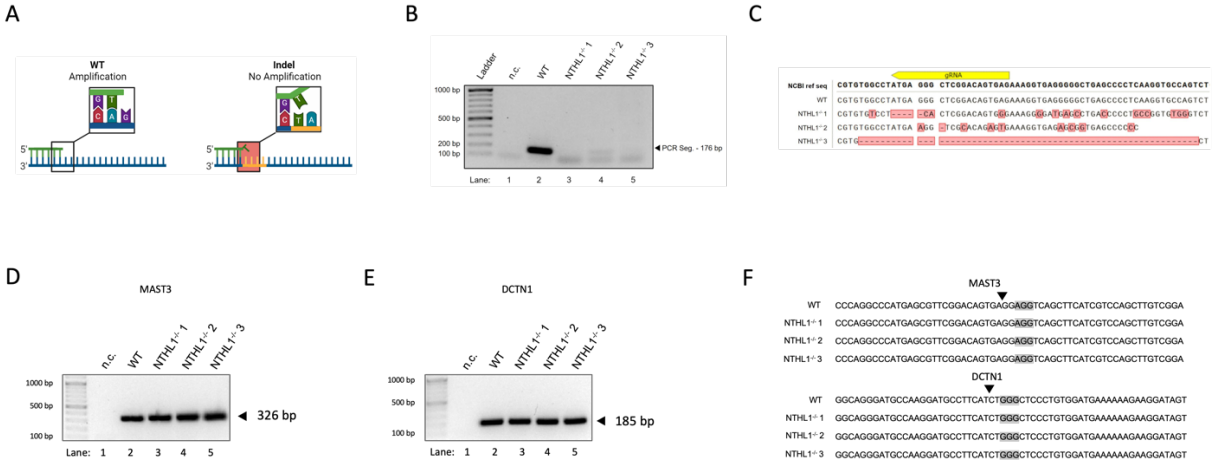

Figure S2: Screening and Quality control of *NTHL1*$^{-/-}$ clones.
(A) Indel-specific PCR: An indel-specific PCR was performed to screen for mutations in NTHL1 knockout clonal cell lines. The PCR does not yield a product in the presence of indel mutations, confirming successful targeting.
(B) Clonal screening: Individual clonal cell lines were isolated and screened for indel mutations in the sgRNA-targeted region of NTHL1 using indel-specific PCR, confirming gene disruption at the DNA level.
(C) Sanger sequencing validation: Indel mutations identified in selected knockout clones were further validated by Sanger sequencing, confirming the precise succesful editing made by CRISPR/Cas9.
(D-F) Off-target analysis: To ensure the specificity of the CRISPR/Cas9 system, potential off-target sites identified by CRISPOR were examined. Exonic off-target regions in MAST3 **(D)** and DCTN1 **(E)** were screened using indel-specific PCR, and the amplified regions were further confirmed to be free of mutations by Sanger sequencing (F).

Figure S3

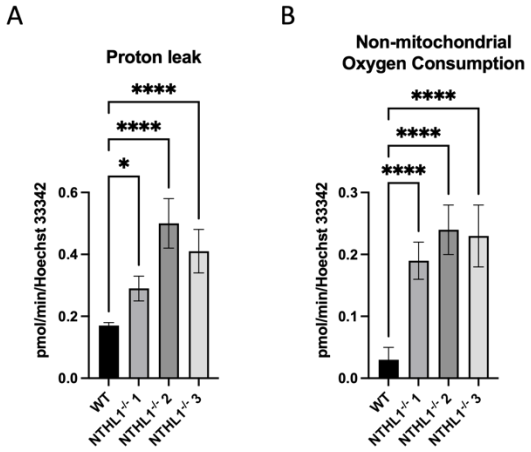

Figure S3: Increased Proton Leak and Non-Mitochondrial Oxygen Consumption in NTHL1-Deficient Cell Lines.
(A) Proton Leak: NTHL1-deficient cells show increased proton leak, indicating energy dissipation as heat instead of ATP production, suggesting altered mitochondrial efficiency.
(B) Non-Mitochondrial Oxygen Consumption: These cells also exhibit increased non-mitochondrial oxygen consumption, reflecting heightened oxidative activity and potential ROS generation outside the mitochondria.

Figure S4

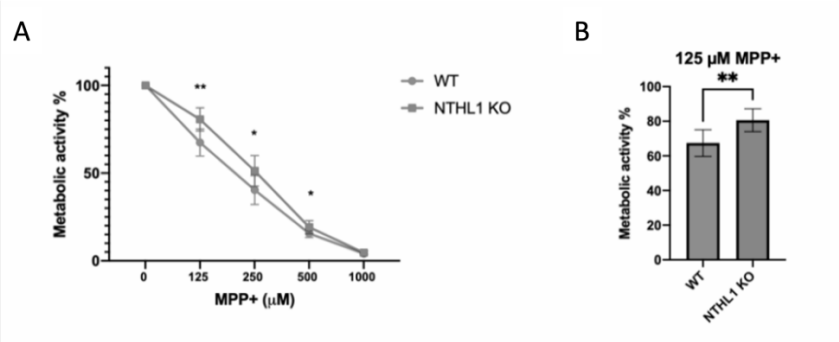

Figure S4. NTHL1-deficient cells display enhanced tolerance to 1-methyl-4 phenylpyridinium (MPP+). Viability of HAP1 WT and NTHL1 KO after 72h treatment with indicated amounts of MPP+ (A-B). Error bars represent mean ± SD (n ≥ 3). Two-tailed Multiple t-tests, ns – nonsignificant, *p ≤ 0.05, **p ≤ 0.01.

Table 1. List of antibodies

Reagent or Resource	**Source**	**Identifier**
Goat Anti-Rabbit IgG Antibody (H+L), HRP	Vector Laboratories	PI-1000-1
Horse Anti-Mouse IgG Antibody (H+L), HRP	Vector Laboratories	PI-2000-1
Mouse Anti-NTH1 antibody [2660C1a]	Abcam	ab70726
Mouse Anti-alpha Tubulin antibody [DM1A], HRP	Abcam	ab40742
Rabbit Histone H3 (D1H2) XP® mAb, HRP	Cell Signaling	12648
Mouse Cytochrome c Apoptosis WB Antibody Cocktail	Abcam	ab110415
Mouse OPA1 Antibody (D-9)	Santa Cruz	sc-393296
Total OXPHOS Rodent WB Antibody Cocktail	Abcam	ab110413
Mitofusion 1+2 antibody (3C9)	Abcam	ab57602
DRP1 Antibody (C-5)	Santa Cruz	sc-271583

Table 2. List of kit and plasmids

Reagent or Resource	**Source**	**Identifier**
Cell Fractionation Kit - Standard	Abcam	ab109719
AllPrep DNA/RNA/Protein Mini Kit	Qiagen	80004
Plasmids		
pCMV6-AC-GFP-NTHL1	Origene	RG214598
pcDNA3-RFP	Addgene	13032

Table. 3 List of primers and sequences

ID	Target	Fw/Rv	Sequence (5'-3')	Assay	Source
RT-qPCR					
	MT-ND6	Fw	CCCCATGCCTCAGGATACTC	RT-qPCR cDNA	
	MT-ND6	Rv	TTGTTAGCGGTGTGGTCGG	RT-qPCR cDNA	
	MT-CYTB	Fw	ACCCCCTAGGAATCACCTCC	RT-qPCR cDNA	
	MT-CYTB	Rv	GCCTAGGAGGTCTGGTGAGA	RT-qPCR cDNA	
	B2M	Fw	AGGCTATCCAGCGTACTCCA	RT-qPCR cDNA	
	B2M	Rv	TGTCGGATGGATGAAACCCA	RT-qPCR cDNA	
	HCCS	Fw	CTGCAGAGTGTCCTTGTGGT	RT-qPCR cDNA	
	HCCS	Rv	AGGCAACTCATACCCCATCC	RT-qPCR cDNA	
	TSPO	Fw	TCAGCCATGGGGTACGGC	RT-qPCR cDNA	
	TSPO	Rv	GTACCAGGCCACGGTAGTG	RT-qPCR cDNA	
	FASN	Fw	GGACACAGTCACCATCTCGG	RT-qPCR cDNA	
	FASN	Rv	GCTCCCGGATCACCTTCTTG	RT-qPCR cDNA	
	ALDH1L2	Fw	AGCCTGGTCTCGTTACCAAAA	RT-qPCR cDNA	
	ALDH1L2	Rv	CCAGCCCAGATGACCTTGA	RT-qPCR cDNA	
	NTHL1 Isoform 1	Fw	GCAACAGCTGGTCAACATCC	RT-qPCR cDNA	
	NTHL1 Isoform 1	Rv	CACCTGGTACCTGCGTACCTTT	RT-qPCR cDNA	
	NTHL1 Isoform 2	Fw	CCCCCCCAAAGAGCAAGGT	RT-qPCR cDNA	
	NTHL1 Isoform 2	Rv	AGCCCACCAAGAGTCCATTG	RT-qPCR cDNA	
	NTHL1 Isoform 3	Fw	GGACAGTGAGAAAGGTACGCA	RT-qPCR cDNA	
	NTHL1 Isoform 3	Rv	ACTGCAATGCCTGACACAGT	RT-qPCR cDNA	
	GAPDH	Fw	CCACATCGCTCAGACACCAT	RT-qPCR cDNA	
	GAPDH	Rv	CCAGGCGCCCAATACG	RT-qPCR cDNA	
	qPCR				
	Mitochondrial Minor arc	Fw	CCGACATCTGGTTCCTACTTCA	qPCR DNA	
	Mitochondrial Minor arc	Rv	AGACCTGTGATCCATCGTGA	qPCR DNA	
	CYTB	Fw	CCCACATCACTCGAGACGTA	qPCR DNA	
	CYTB	Rv	CCGATGTTTCAGGTTTCTGAGTA	qPCR DNA	

	B2M	Fw	GCTGGGTAGCTCTAAACAATGTATTCA	qPCR DNA	
	B2M	Rv	CCATGTACTAACAAATGTCTAAAATGGT	qPCR DNA	
	MT-RNR1	Fw	ACCTGGCGGTGCTTCATATC	RADF, DNA	[29]
	MT-RNR1	Rv	GGCTATCGTAGTTTTCTGGGGTA	RADF, DNA	
	MT-RNR2	Fw	CTTCACCAGTCAAAGCGAACT	RADF, DNA	
	MT-RNR1	Rv	TAGCGGCTGCACCATCG	RADF, DNA	
	mtDNA	Fw	TCTAAGCCTCCTTATTCGAGCCGA	Long Amp PCR	[45]
	mtDNA	Rv	TTTCATCATGCGGAGATGTTGGAT GG	Long Amp PCR	
	Side directed mutagenesis				
	NTHL1-FLAG	Fw	tacaaggacgacgacgacaagtgaTAATCTAGA GGGCCCTATTCTATAGTGTCACC	SDM	
	NTHL1-FLAG	Rv	gtcgatgtcgtggtccttgtagtcaccgtcgtggtcct tgtagtcCTCGAGCGGCCGCGT	SDM	
CRISPR/Cas9					
	NTHL1 SgRNA	-	CTCACTGTCCGAGCCCTCAT AGG	SgRNA + PAM	
	MAST3 off target	-	CTCACTGTCCGAACGCTCAT	Off target	
	DCTN1 off target	-	CTCACTGCCAGGGCCCTCAT	Off target	
	NTHL1_indel_Fw_1	Rv	CCAAAAGCCACCGGGTAGAA	Indel PCR	
	NTHL1_indel_Rv	Rv	AACGAGTGAGGGGTGAGCTA	Indel PCR	
	NTHL1_indel_Fw_2	Fw	CTCACTGTCCGAGCCCTC	sequencing	
	NTHL1_Fw	Fw	CCAAAAGCCACCGGGTAGAA	PCR and Indel	
	NTHL1_Rv	Rv	AACGAGTGAGGGGTGAGCTA	PCR	
	NTHL1_Fw_Seq	Fw	TTCCTCATGGCACGGATGTT	Sequencing	
	NTHL1_Rv_Indel	Rv	CTCACTGTCCGAGCCCTC	Indel	
	MAST3_Fw	Fw	GCAGGATGTGCGTGGTTTTT	PCR and Indel	
	MAST3_Rv	Rv	ACACGATGGGAACTGTCACC	PCR	
	MAST3_Fw_Seq	Fw	GGTTTTGCATGCAGTGGGAC	Sequencing	
	MAST3_Rv_Indel	Rv	CTCACTGTCCGAACGCTC	Indel	
	DCTN1_Fw	Fw	AGAACACTGCTGGGAAGAGC	PCR and Indel	
	DCTN1_Rv	Rv	GGAGGACTGGGATGGGAGAT	PCR	
	DCTN1_Fw_Seq	Fw	GCTGGTGCGAGTGATGTCTA	Sequencing	
	DCTN1_Rv_Indel	Rv	CTCACTGCCAGGGCCCTC	Indel	